PROCEEDINGS OF SPIE

SPIEDigitalLibrary.org/conference-proceedings-of-spie

A high dynamic range imaging method for the characterization of periodic errors in diffraction gratings

Sofia C. Corzo-Garcia, Muhammad Imran Afzal, Benjamin T. Kidder, Michelle A. Grigas, Ulf Griesmann

Sofia C. Corzo-Garcia, Muhammad Imran Afzal, Benjamin T. Kidder, Michelle A. Grigas, Ulf Griesmann, "A high dynamic range imaging method for the characterization of periodic errors in diffraction gratings," Proc. SPIE 10750, Reflection, Scattering, and Diffraction from Surfaces VI, 1075009 (4 September 2018); doi: 10.1117/12.2321227

SPIE.

Event: SPIE Optical Engineering + Applications, 2018, San Diego, California, United States

Downloaded From: https://www.spiedigitallibrary.org/conference-proceedings-of-spie on 2/15/2019 Terms of Use: https://www.spiedigitallibrary.org/terms-of-use

A High Dynamic Range Imaging Method for the Characterization of Periodic Errors in Diffraction Gratings

Sofia C. Corzo-Garcia[a], Muhammad Imran Afzal[b], Benjamin T. Kidder[c], Michelle A. Grigas[c], and Ulf Griesmann[a]

[a]National Institute of Standards and Technology (NIST), Physical Measurement Laboratory, Gaithersburg, MD 20899-8220, USA
[b]Department of Biomedical Science and Engineering, Gwangju Institute of Science and Technology, Buk-gu, Gwangju, 61005, South Korea
[c]University of Texas at Austin, Department of Astronomy, Austin, TX 78712-1205, USA

ABSTRACT

We report on recent progress in the development of our focal plane imaging system for the detection and characterization of small fabrication errors in diffraction gratings. The instrument uses a purpose-designed high dynamic range imaging method in conjunction with a low-cost digital camera to acquire images with a dynamic range that can now exceed eight orders of magnitude. The sensitivity and utility of the instrument is demonstrated with measurements of three different diffraction gratings. Avenues for further possible improvements of the instrument are discussed.

Keywords: Diffraction gratings, High dynamic range imaging, Fabrication errors

1. INTRODUCTION

Diffraction gratings are widely used dispersive optical elements in applications that require knowledge of the spectral composition of light. All fabrication processes used to make diffraction gratings impart characteristic fabrication errors to a diffractive optical surface. These errors often have a spatial period because large grating surfaces must be patterned incrementally in a step-and-repeat fashion, and such periodic errors can result in spurious spectral information ("ghosts") or increased levels of scattered light ("grass") in the spectrometers that use the gratings.[1]

The work summarized in this paper has its origin in a collaboration of the University of Texas at Austin and NIST with the goal to improve the fabrication process of silicon immersion echelle gratings for remote sensing applications in the infrared.[2] Silicon immersion gratings enable the design of compact spectrometers for the infrared with very high spectral resolution.[3–5] Echelle gratings can be fabricated on silicon substrates using a lithographic process and by taking advantage of the well known anisotropic etch behavior of silicon in a concentrated potassium hydroxide (KOH) solution.[6] A substrate is cut from a silicon boule with a crystal plane orientation such that the KOH etch creates grating structures with the correct slope for the desired blaze angle. The grating structure is defined on the silicon substrate by a silicon nitride mask, which is insoluble in the KOH solution. This hardmask is patterned with a lithographic process using either contact lithography[5] or a form of direct-write lithography.[2]

The fabrication tolerances of immersed silicon gratings are a persistent challenge. While the immersion of a grating in a material provides the benefit of increasing its spectral dispersion, the fabrication tolerances for the gratings are lowered by the same factor. Fabrication tolerances become especially tight for echelle gratings because the tolerances scale with $1/m$ where m is the diffraction order. For example, periodic grating line positioning errors must not exceed a few nm to ensure that Rowland ghosts are kept at an acceptable level.[3,5]

In our work at NIST we are using a direct-write photolithography system[7] to pattern a silicon nitride hardmask on substrates for silicon immersion gratings, an approach that circumvents several of the problems encountered in contact lithography.[5] We found that we needed an instrument to identify and evaluate fabrication errors that enables us to optimize the lithographic fabrication process so that the levels of "ghosts" and scattered light in the finished gratings are as low as possible.

Author contact emails: sofia.corzo@nist.gov

Reflection, Scattering, and Diffraction from Surfaces VI, edited by Leonard M. Hanssen, Proc. of SPIE Vol. 10750, 1075009 · © 2018 SPIE · CCC code: 0277-786X/18/$18 · doi: 10.1117/12.2321227

Downloaded From: https://www.spiedigitallibrary.org/conference-proceedings-of-spie on 2/15/2019
Terms of Use: https://www.spiedigitallibrary.org/terms-of-use

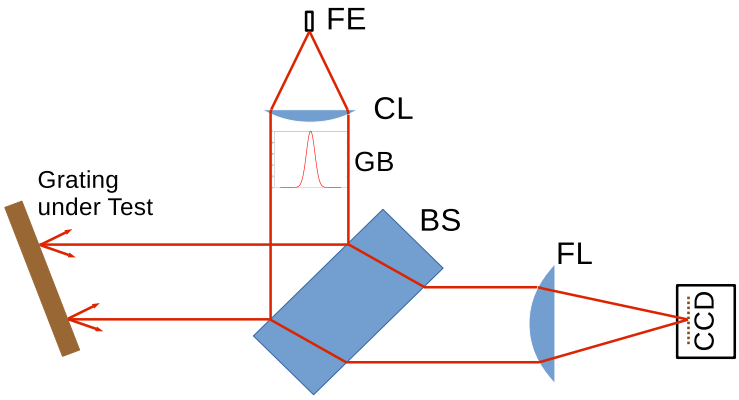

Figure 1: Concept of our instrument for the analysis of fabrication errors in diffraction gratings. The chief components of the instrument are a fiber end light source (FE), a collimator lens (CL), Gaussian beam (GB), a beam splitter (BS), a focusing lens (FL), and a camera with charge-coupled device (CCD) image sensor.

The instrument we are developing has conceptual roots in techniques that were developed for the assessment of ruled diffraction gratings. An example are those developed at the Mount Wilson Observatory.[8] Similar methods were used recently in an instrument that was developed for the detection of Rowland ghosts in gratings fabricated with e-beam lithography.[9] Our instrument is set apart by the use of a digital camera instead of a photomultiplier as detector. We demonstrate in section 4 that modern solid state image sensors combined with a high dynamic range imaging method can achieve a dynamic range that may eventually approach that of photomultipliers. Solid state image sensors have the advantage that they provide a two-dimensional image of ghosts and stray light with high angular resolution in the vicinity of a diffraction order instead of a one-dimensional profile, and they are low in cost.

In section 2 we describe the basic design of our instrument. A high dynamic range (HDR) imaging method is central to our instrument and it is summarized in section 3. Measurements for three different diffraction gratings are shown in section 4 to demonstrate the utility and capability of our instrument for the identification and characterization of fabrication errors.

2. INSTRUMENT DESIGN

The instrument we describe in this paper is, in essence, an autocollimator[10,11] combined with a high dynamic range camera. The concept is illustrated in Fig. 1. A frequency stabilized helium-neon laser operating at a wavelength of $632.8\,\mathrm{nm}$ is used as the light source for the autocollimator. Gratings are dispersive optical elements and a source with very narrow spectral line width is required. The light from the laser is coupled into a single-mode optical fiber which provides a convenient way to transmit the light to the experimental setup inside a light-tight box. The adjustable fiber coupler also gives us a simple means for varying the optical power to avoid saturation of the camera.

A lens (CL in Fig. 1) collimates the light emitted by the optical fiber end to create a collimated Gaussian beam (GB in Fig. 1) with a $1/e^2$ width of $11\,\mathrm{mm}$. The collimator aperture has a diameter of $25\,\mathrm{mm}$, sufficiently large to ensure that diffraction effects are minimal. A plate beam splitter directs half of the light towards the grating under test. The transmitted fraction of the beam is absorbed by a beam stop made of a black felt material. The beam splitter has a substrate made from silica glass with a diameter of $75\,\mathrm{mm}$ and a thickness of $25\,\mathrm{mm}$. The beam splitter coating has a transmittance to reflectance ratio of one. The reverse side of the beam splitter is coated with a v-type anti-reflection coating to minimize stray light caused by the back surface reflection. Using a plate beam splitter instead of a beam splitter cube is an important improvement over our initial prototype design.[12] The grating under test is mounted in a 5-axis mount and oriented such that the beam from the beam splitter is reflected at the angle of incidence (Littrow position). All measurements described in this paper were made at the first diffraction order. The fraction of the beam reflected by the grating that traverses the beam splitter is focused onto the surface of a charge coupled device (CCD) image sensor by a lens with a focal length of $100\,\mathrm{mm}$. In the experimental setup we describe here the focusing lens is a simple plano-convex spherical lens with a diameter of $50\,\mathrm{mm}$. The lens surfaces are coated with v-type anti-reflection coatings for the laser wavelength.

Downloaded From: https://www.spiedigitallibrary.org/conference-proceedings-of-spie on 2/15/2019
Terms of Use: https://www.spiedigitallibrary.org/terms-of-use

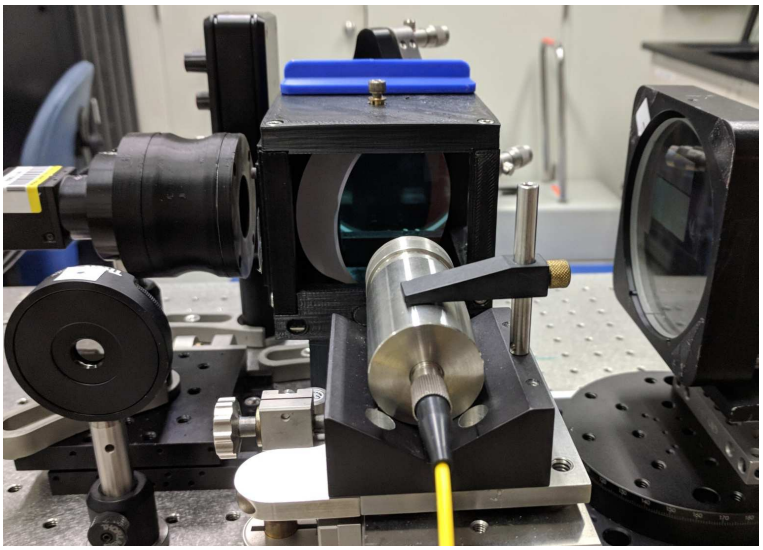

Figure 2: Photo of a measurement setup.

The camera in our current instrument is an uncooled mid-range industrial vision camera with a CCD sensor that has 2448×2048 square pixels of $3.45\,\mu\mathrm{m}$ width. The analog-to-digital converter of the camera has a resolution of 12 bits. Camera exposure times can be programmed between $100\,\mu\mathrm{s}$ and $32\,\mathrm{s}$. The camera has a programmable amplifier with a variable gain between 0.1 and 15. Both the window in the camera housing and also the coverglass protecting the sensor chip were removed because the windows were a dominant cause of stray light in our initial measurements. CCD sensors reflect a significant fraction of light that impinges on their surface and because the sensor surface is a grid of pixels, which cause reflected light to be scattered into a wide range of angles. A sensor cover glass would reflect part of the reflected light back towards the sensor, thus causing a large background signal when the camera is operating at high sensitivity with high gains and large exposure times.

A photograph of a measurement setup is shown in Fig. 2, which shows the instrument from the side of the laser beam collimator (top of Fig. 1). The beam splitter in its mount is at the center of the image. The grating to the right is a computer generated hologram that was fabricated at NIST for the form measurement of an elliptical mirror.[13] A micrograph of the grating is shown in Fig. 3b. The focusing lens is integrated into the beam splitter mount and the camera can be seen on the left side of the image. Several strategies were applied to reduce the level of stray light. A light trap in front of the camera reduces the amount of stray light that can reach the camera sensor. Parts of the beam splitter mount that are exposed to diffracted light from the grating under test are covered with a black light-absorbing foil to reduce the amount of light scattered in the direction of the camera sensor. During measurements the entire setup is enclosed in a light-tight box made from black foam board to eliminate room light and reduce the level of stray light.

3. HIGH DYNAMIC RANGE IMAGING

High dynamic range (HDR) imaging has become possible even with low-cost digital cameras and an HDR imaging method is at the heart of the instrument we are describing here. An HDR image is constructed from a sequence of images that were acquired with increasing camera sensitivity. In a typical measurement the camera is first set to its lowest sensitivity with the lowest gain and the shortest exposure time, the laser power is adjusted such that the peak pixel value is just below the 12 bit saturation level, and an initial image, I^1 with pixels I^1_{ij} is acquired, where i and j denote the horizontal and vertical pixel position in the image. A sequence of images $\{I^k : k = 1 \ldots N\}$ with increasing camera gains g_k and exposure times τ_k is then acquired. All images except the first image have pixels at or close to the saturation level of the camera and these pixels are considered invalid for the construction of the HDR image. All images I^k can be scaled to a common intensity scale by multiplying them with a weight factor, w_k, derived from the exposure time τ_k and camera gain factor g_k:

$$w_k = \frac{g_1 \tau_1}{g_k \tau_k} \,. \tag{1}$$

Downloaded From: https://www.spiedigitallibrary.org/conference-proceedings-of-spie on 2/15/2019
Terms of Use: https://www.spiedigitallibrary.org/terms-of-use

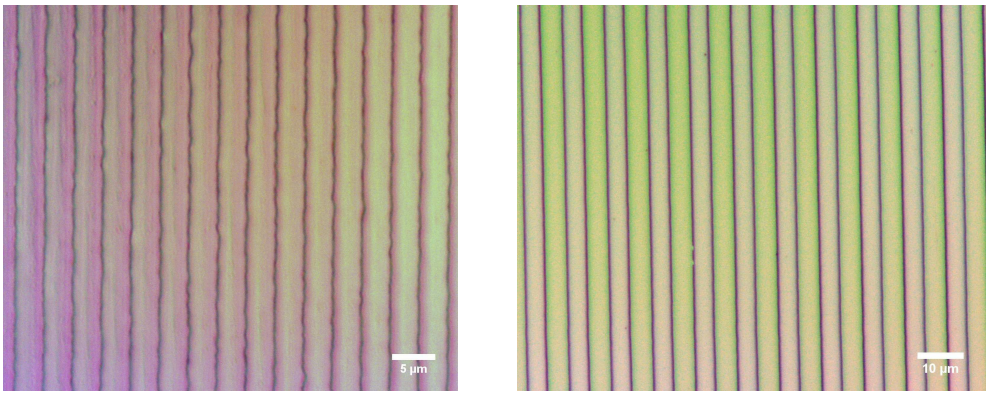

(a) (b)

Figure 3: Bright field microscope images of a mechanically ruled blazed grating (a) and a computer generated hologram etched into a glass substrate (b). The scale bar lengths are $5\,\mu\mathrm{m}$ for image (a) and $10\,\mu\mathrm{m}$ for image (b).

An HDR image, H, is computed as the weighted average of all images I^k in an image sequence as follows:

$$H_{ij} = \frac{1}{n_{ij}} \sum_{k=1}^{n_{ij}} w_k \cdot I_{ij}^k \,, \tag{2}$$

where w_k are the weight factors defined in Eq. 1, and the sum denotes a pixel-by-pixel sum of the images. In each image sequence only valid pixels with values below a threshold level close to the saturation level of the camera are included in Eq. 2, and n_{ij} represents the number of valid measurements at pixel (i, j). For the results presented in section 4 image sequences with 24 images were acquired.

The uncooled camera has a substantial amount of dark noise, which originates from thermally generated currents within the CCD sensor. The level of dark noise was measured with a covered sensor for all gain and exposure time settings of the camera. The dark noise in an image was found to be between 6 and 7 bits with only weak dependence on camera gain and exposure time. Slightly larger noise values were observed for larger exposure times. For most of our measurements each of the images I_k in a sequence is an average of 10 images, all acquired at the same gain and exposure time. The noise floor from each average image except the one that was acquired with the largest gain and exposure time is then removed by marking all pixels with values below a certain threshold value (e.g. 110, which is slightly below the 6 bits of noise) as invalid before computing the HDR image using Eq. 2.

4. MEASUREMENT EXAMPLES

The first of our examples is a reflection grating that is mechanically ruled into an aluminum layer on a glass substrate. The grating has a groove density of 300 lines/mm and a blaze angle of $11°$. A bright-field micrograph of the ruled grating surface is shown in Fig. 3a. Fig. 4a shows the corresponding focal plane image for the mechanically ruled grating. The arrow in this and the other focal plane images points to a reflection from the back surface of the beam splitter. The grating is aligned to locate the signal peak at the center of the image sensor. We normalize all focal plane images such that the signal peak has a magnitude of one. The most striking feature in Fig. 4a is a horizontal band of scattered light (slightly rotated due to sub-optimal alignment of the grating in its mount). A close look at the micrograph of the grating surface in Fig. 3a reveals the cause for the scattered light. The plowing action of the diamond tool that was used in the ruling process did not create grooves with precisely defined width. Some of the material is pushed to one side of the grooves by the tool thus, essentially, adding a random component to the width of the grating grooves. This results in a small fraction of light being reflected into randomized angles.

Details can be difficult to discern in the focal plane images. Fig. 5 shows a horizontal (blue line in 5a) – actually in the direction of the scattered light band in Fig. 4) – and an orthogonal section in vertical direction (5b). In the horizontal section Rowland ghosts are clearly visible near the central peak. These are most likely caused by a periodic error in the mechanism that advances the diamond tool from groove to groove during the ruling process. The red line in Fig. 5a is a

Downloaded From: https://www.spiedigitallibrary.org/conference-proceedings-of-spie on 2/15/2019
Terms of Use: https://www.spiedigitallibrary.org/terms-of-use

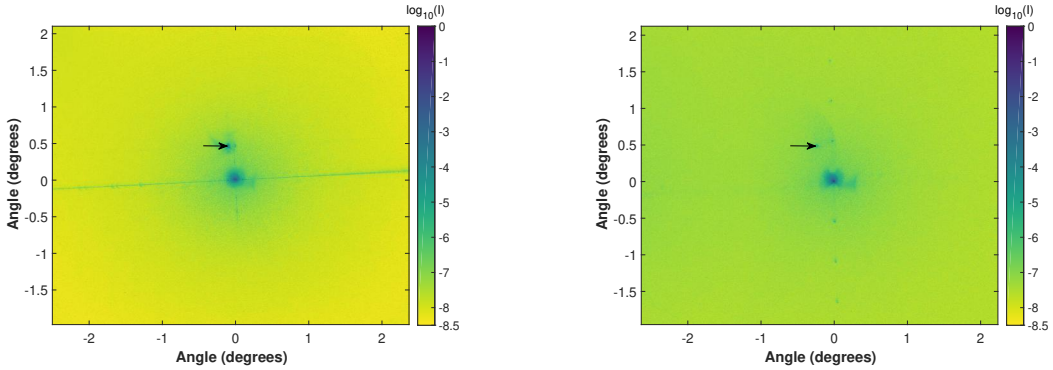

(a) (b)

Figure 4: HDR images at the focal plane of the focusing lens of light reflected in the first diffraction orders by the ruled grating (a) and the computer generated hologram (b) shown in Fig. 3. The arrows point to a reflection from the back surface of the beam splitter.

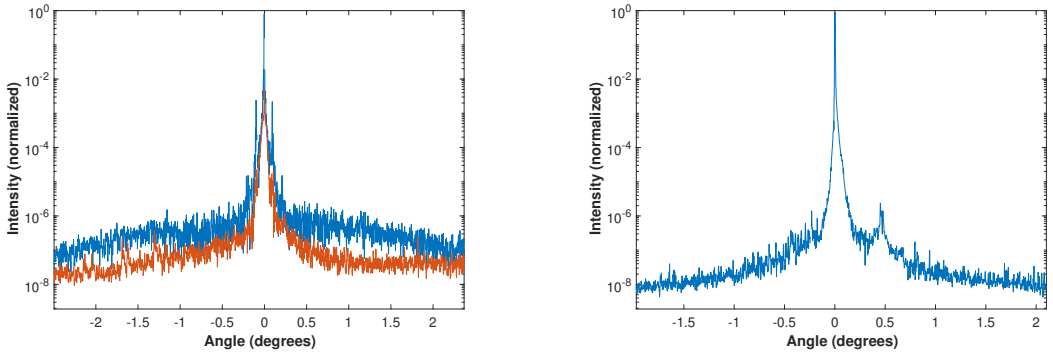

(a) (b)

Figure 5: Central sections in horizontal (a) and vertical (b) directions of the image in Fig. 4a for the ruled grating in Fig. 3a.

section in the same direction as the blue line, but offset in vertical direction from the center by -4 pixels. This slightly offset section was added in Fig. 5a to show that peaks with low signal-to-noise ratio are present between -1° and -2° that have no corresponding peaks at positive angles. The origin of these peaks is currently unclear. In the vertical section, Fig. 5b, no ghosts are visible at the signal-to-noise ratio that we can currently achieve. The asymmetry of the central peak is due to aberrations caused by the focusing lens. The peak at 0.5° is caused by a stray reflection at the back surface of the beam splitter.

A different grating is shown in Fig. 3b. This grating is a computer generated hologram that was developed and fabricated at NIST for an interferometric measurement of the form error of an elliptical mirror.[13] This hologram is a transmission phase grating that was etched into a borosilicate glass substrate. The nominal duty cycle of the grating is 50%, although in the actual grating the valleys are slightly wider than the ridges. The grating grooves are very nearly straight. Compared to the ruled grating in Fig. 3a the grating grooves are much better defined with far less line edge roughness. This is also evident in the focal plane image Fig. 4b, which does not have the prominent band of scattered light that characterizes the focal plane image for the ruled grating. The horizontal section in Fig. 6a shows a weak indication of Rowland ghosts but at a much lower level than in the ruled grating. The small peak to the right of the central peak in Fig. 6a is caused by a stray reflection off the back surface of the transparent glass substrate. Even though an absorber was bonded to the back surface of the hologram, it does not fully suppress the back surface reflection. A vertical section through the center of the focal plane image Fig. 4b is shown in Fig. 6b. The ghosts in Fig. 6b clearly show the presence of a periodic error in the vertical direction of the hologram depicted in Fig. 3b, even though periodic errors are not recognizable in micrographs of the hologram surface. The cause for the periodic error is clear. The hologram shown in Fig. 3b was fabricated with a lithography tool that patterned the hologram in a photoresist by sequentially exposing horizontal strips of about $65\,\mu\mathrm{m}$ width. This incremental exposure process results in a periodic error in vertical direction of the hologram pattern in Fig. 3b

Downloaded From: https://www.spiedigitallibrary.org/conference-proceedings-of-spie on 2/15/2019
Terms of Use: https://www.spiedigitallibrary.org/terms-of-use

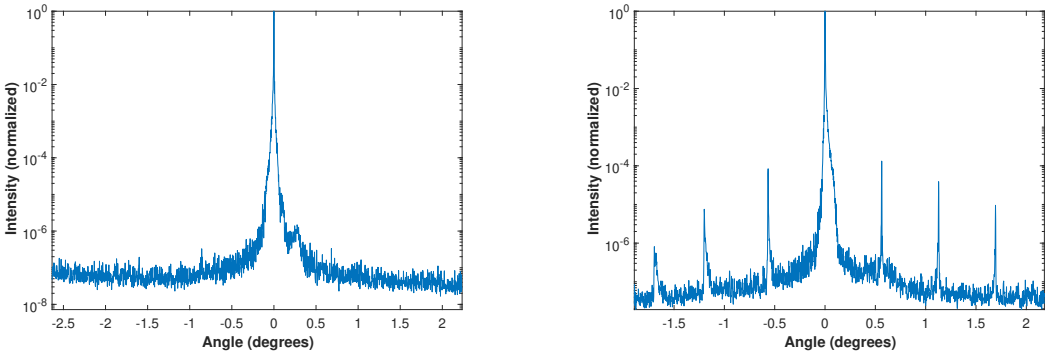

(a) (b)

Figure 6: Central sections in horizontal (a) and vertical (b) directions of the image in Fig. 4b for the computer generated hologram in Fig. 3b.

due to an exposure dose error at the boundaries of adjacent strips. From the spacing of the diffraction orders in Fig. 3b we calculate a spatial period of the exposure error of $64.3\,\mu\mathrm{m}$. The measurements in Figs. 5 and 6 illustrate the sensitivity of the focal plane imaging method for the detection of small periodic errors in gratings.

A third example illustrates the usefulness of the focal plane imaging method to assist in the fabrication of immersed silicon gratings.[4] In the lithographic fabrication of immersed silicon echelle gratings a lithographic process is used to pattern a silicon nitride hard mask that is insoluble in KOH before the grating grooves are wet etched in the KOH solution. Any patterning errors in the hard mask will, after KOH etching, result in corresponding defects in the finished immersion grating. Fig. 7a is a bright-field micrograph, acquired with differential interference contrast, of a silicon nitride hard mask on a silicon test wafer. In the image the silicon nitride lines appear dark, the brighter areas are blank silicon. The silicon nitride layer is about $50\,\mathrm{nm}$ thick and was patterned with the same direct-write photolithography system that was used to fabricate the hologram shown in Fig. 3b. The corresponding focal plane image can be seen in Fig. 7b. This echelle grating has a lower groove density than the gratings in Fig. 3 and, consequently, the angular separation of the diffraction orders is smaller. Three diffraction orders are in the field of view of the image sensor. The wafer is also not as flat as the substrates of the gratings in Fig. 3, making the wavefronts reflected by the wafer more aberrated in addition to the aberrations introduced by the focusing lens. Horizontal and vertical sections through the center of the first order diffraction peak in Fig. 7b are shown in Fig. 8. As in the case of the hologram in Fig. 3b, the dominant ghosts occur in vertical direction and, as before, they can be traced to the incremental step-and-expose action of the lithography system. In this case the exposed bands were wider than for the hologram in Fig. 3b, which explains why the ghosts in Fig. 8b are more closely spaced. The relative ghost intensity for the patterned silicon nitride hard mask is about 20 times higher than it was for the hologram (see Fig. 6b). The cause was found in a less-than-optimal setup of the lithography system that resulted in a small, periodic exposure dose variation in the direction of the grating lanes. The HDR focal plane imager is a very sensitive tool for the optimization of the the lithography tool setup and of the lithographic exposure process.

Even a cursory look at the focal plane images in Figs. 4 and 7b shows that the background noise level in the images is strikingly different. The noise floor for the silicon nitride grating on the silicon wafer in Fig. 7b is approximately 100 times higher than that for the ruled grating in Fig. 4a. A qualitative explanation for the variation in the noise level emerges when the distribution of light into the different diffraction orders by the gratings is considered. All gratings were measured in the first diffraction order. The gratings distribute light into several diffraction orders differently, and this can strongly affect the level of stray light in the measurements. The ruled grating is blazed for the first diffraction order and it creates the least stray light at the unwanted diffraction orders, and the focal plane image Fig. 4a has the highest signal-to-noise ratio. The hologram is a binary grating that distributes more light into a wider range of diffraction orders than the blazed grating. Contrary to its design, the hologram was also tested in reflection, which causes a substantial reflection in the zeroth order, that further increases the stray light level. Finally, the silicon nitride grating with only $50\,\mathrm{nm}$ structure height and a duty cycle of only about 30% has very low diffraction efficiency. A powerful reflection is present in the zeroth diffraction order which is difficult to separate from the higher diffraction orders because of the low groove density of the grating. This strong reflection is the likely cause for the much higher noise level in Fig. 7b.

Downloaded From: https://www.spiedigitallibrary.org/conference-proceedings-of-spie on 2/15/2019
Terms of Use: https://www.spiedigitallibrary.org/terms-of-use

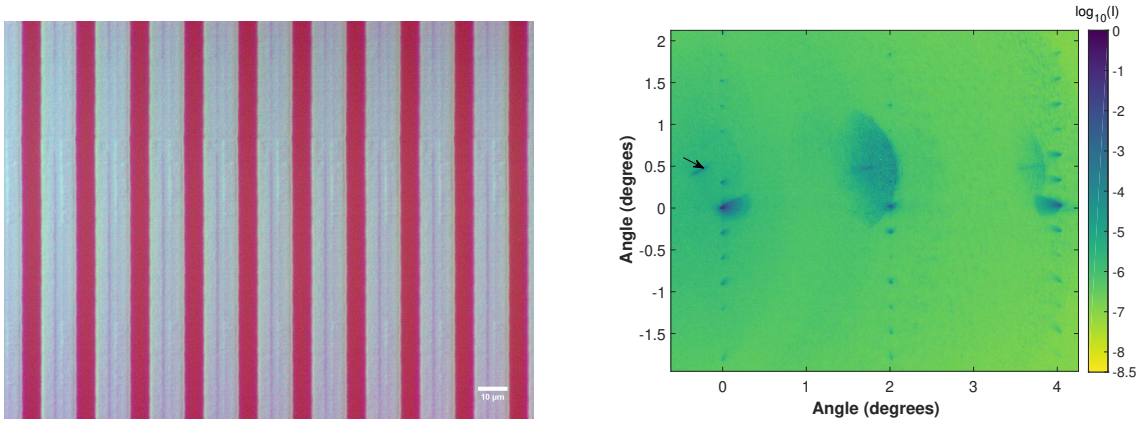

(a) (b)

Figure 7: Micrograph in differential interference contrast of a silicon nitride hardmask for the etching of an echelle grating on a silicon wafer (a) and focal plane image of lowest diffraction orders (b). The first, second, and third diffraction orders are visible in the image, the first order is on the left in Fig. b. The crescent-shaped feature at the center of the image is likely light from the very strong 0^{th} order that was scattered by the mount of the focusing lens. The scale bar in Fig. a has a length of $10\,\mu\text{m}$.

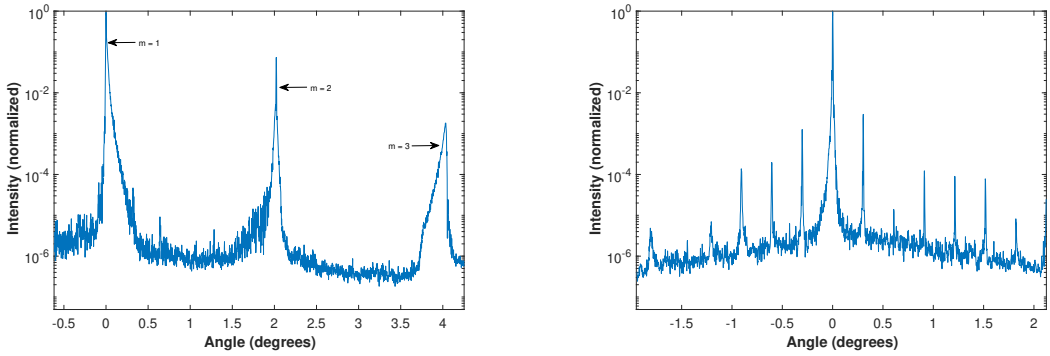

(a) (b)

Figure 8: Central sections in horizontal direction (a) and vertical (b) direction for the first diffraction order in the image shown in in Fig. 7b.

5. CONCLUSIONS

Our measurements demonstrate that a rather simple focal plane imaging system using a low cost camera with a high dynamic range imaging method can be used as a sensitive detector for fabrication errors in gratings. The focal plane imaging method seems to be significantly more sensitive than direct microscopic inspection of the gratings. Our instrument is currently able to achieve a dynamic range of slightly above eight orders of magnitude, which is an increase by a factor of about 16 over our prototype instrument.[12] One clear conclusion that can be drawn from the measurements presented here is that stray light management is critically important to enable measurements with high signal-to-noise ratio. Another revision of the instrument design is now being implemented with the goal to further reduce the stray light level. Additional improvements are underway that will enable precise control of the laser power which, in turn, will allow us to reduce the measurement time. One question that is currently unanswered is the degree of linearity of the imaging system and we are exploring several ways in which the linearity of the imaging over the whole dynamic range of the instrument can be tested.

Acknowledgments

This work was supported by NASA APRA grants NNH15AB221 to NIST and NNX15AD97G to the University of Texas. The lithography work done at NIST relied, in part, on tools and processes available at NIST's Center for Nanoscale Science and Technology (CNST).

Downloaded From: https://www.spiedigitallibrary.org/conference-proceedings-of-spie on 2/15/2019
Terms of Use: https://www.spiedigitallibrary.org/terms-of-use

REFERENCES

[1] Harrison, G. R., "The challenge of the ruled grating," *Physics Today* **3**, 6–12 (sep 1950).

[2] Brooks, C. B., Kidder, B., Grigas, M. A., Griesmann, U., Wilson, D. W., Muller, R. E., and Jaffe, D. T., "Process improvements in the production of silicon immersion gratings," *Proc. SPIE* **9912**, 99123Z (2016).

[3] Marsh, J. P., Mar, D. J., and Jaffe, D. T., "Production and evaluation of silicon immersion gratings for infrared astronomy," *Applied Optics* **46**(17), 3400–3416 (2007).

[4] Wang, W., Gully-Santiago, M., Deen, C., Mar, D. J., and Jaffe, D. T., "Manufacturing of silicon immersion gratings for infrared spectrometers," in [*Modern Technologies in Space- and Ground-based Telescopes and Instrumentation*], SPIE (jul 2010).

[5] Brooks, C. B., Gully-Santiago, M., Grigas, M., and Jaffe, D. T., "New metrology techniques improve the production of silicon diffractive optics," in [*Advances in Optical and Mechanical Technologies for Telescopes and Instrumentation*], Navarro, R., Cunningham, C. R., and Barto, A. A., eds., SPIE (jul 2014).

[6] Williams, K. and Muller, R., "Etch rates for micromachining processing," *Journal of Microelectromechanical Systems* **5**(4), 256–269 (1996).

[7] Smith, H. I., Walsh, M. I., Zhang, F., Ferrera, J., Hourihan, G., Smith, D., Light, R., and Jaspan, M., "An innovative tool for fabricating computer-generated holograms," *Journal of Physics: Conference Series* **415**(1), 012037 (2013).

[8] Babcock, B. and Babcock, H. W., "The ruling of diffraction gratings at the Mount Wilson Observatory," *J. Opt. Soc. Am* **41**, 776–786 (1951).

[9] Heusinger, M., Banasch, M., Flügel-Paul, T., and Zeitner, U.-D., "Investigation and optimization of Rowland ghosts in high efficiency spectrometer gratings fabricated by e-beam lithography," *Proc. SPIE* **9759**, 97590A (2016).

[10] Malacara, J. Z., "Angle, distance, curvature, and focal length measuerments," in [*Optical Shop Testing, 2nd Edition*], Malacara, D., ed., 715–741, Wiley, New York (1992).

[11] Steel, W. H., "The autostigmatic microscope," *Opt. Laser Eng.* **4**, 217–227 (1983).

[12] Afzal, M. I., Corzo-Garcia, S. C., and Griesmann, U., "A focal plane imager with high dynamic range to identify fabrication errors in diffractive optics," in [*Optical Design and Fabrication 2017 (Freeform, IODC, OFT)*], *Optical Design and Fabrication 2017 (Freeform, IODC, OFT)* , OW3B.2, Optical Society of America (2017).

[13] Griesmann, U., Wang, Q., Soons, J. A., and Assoufid, L., "Figure metrology for x-ray focusing mirrors with Fresnel holograms and photon sieves," in [*Classical Optics 2014*], OSA (2014).

Downloaded From: https://www.spiedigitallibrary.org/conference-proceedings-of-spie on 2/15/2019
Terms of Use: https://www.spiedigitallibrary.org/terms-of-use